AIP Journal of Applied Physics

Potential variations around grain boundaries in impurity-doped BaSi2 epitaxial films evaluated by Kelvin probe force microscopy

D. Tsukahara, M. Baba, S. Honda, Y. Imai, K. O. Hara, N. Usami, K. Toko, J. H. Werner, and T. Suemasu

Citation: Journal of Applied Physics **116**, 123709 (2014); doi: 10.1063/1.4896760
View online: http://dx.doi.org/10.1063/1.4896760
View Table of Contents: http://scitation.aip.org/content/aip/journal/jap/116/12?ver=pdfcov
Published by the AIP Publishing

Potential variations around grain boundaries in impurity-doped $BaSi_2$ epitaxial films evaluated by Kelvin probe force microscopy

D. Tsukahara,[1] M. Baba,[1] S. Honda,[1] Y. Imai,[1,2] K. O. Hara,[3,4] N. Usami,[3,4] K. Toko,[1] J. H. Werner,[5] and T. Suemasu[1,4,5]
[1]*Institute of Applied Physics, University of Tsukuba, Tsukuba, Ibaraki 305-8573, Japan*
[2]*AIST, Tsukuba, Ibaraki 305-8565, Japan*
[3]*Graduate School of Engineering, Nagoya University, Nagoya 464-8603, Japan*
[4]*Japan Science and Technology Agency, CREST, Chiyoda, Tokyo 102-0075, Japan*
[5]*Institute for Photovoltaics, University of Stuttgart, Stuttgart 70569, Germany*

(Received 22 August 2014; accepted 18 September 2014; published online 29 September 2014)

Potential variations around the grain boundaries (GBs) in antimony (Sb)-doped n-type and boron (B)-doped p-type $BaSi_2$ epitaxial films on Si(111) were evaluated by Kelvin probe force microscopy. Sb-doped n-$BaSi_2$ films exhibited positively charged GBs with a downward band bending at the GBs. The average barrier height for holes was approximately 10 meV for an electron concentration $n \approx 10^{17}\,cm^{-3}$. This downward band bending changed to upward band bending when n was increased to $n = 1.8 \times 10^{18}\,cm^{-3}$. In the B-doped p-$BaSi_2$ films, the upward band bending was observed for a hole concentration $p \approx 10^{18}\,cm^{-3}$. The average barrier height for electrons decreased from approximately 25 to 15 meV when p was increased from $p = 2.7 \times 10^{18}$ to $p = 4.0 \times 10^{18}\,cm^{-3}$. These results are explained under the assumption that the position of the Fermi level E_f at GBs depends on the degree of occupancy of defect states at the GBs, while E_f approached the bottom of the conduction band or the top of the valence band in the $BaSi_2$ grain interiors with increasing impurity concentrations. In both cases, such small barrier heights may not deteriorate the carrier transport properties. The electronic structures of impurity-doped $BaSi_2$ are also discussed using first-principles pseudopotential method to discuss the insertion sites of impurity atoms and clarify the reason for the observed n-type conduction in the Sb-doped $BaSi_2$ and p-type conduction in the B-doped $BaSi_2$. © *2014 AIP Publishing LLC*.
[http://dx.doi.org/10.1063/1.4896760]

I. INTRODUCTION

Photovoltaic solar cell materials, such as Si, Cu(In,Ga)Se_2 (CIGS), CdTe, and III-V compound semiconductors have been extensively studied. At the same time, intensive efforts have been made to explore different materials other than the above conventional materials. Among such materials, we have specifically targeted realizing pn junction solar cells using semiconducting barium disilicide ($BaSi_2$). Composed of earth-abundant elements, $BaSi_2$ is an indirect band gap semiconductor with a band gap of approximately 1.3 eV, and has large absorption coefficients exceeding $3 \times 10^4\,cm^{-1}$ for photon energies higher than 1.5 eV.[1–4] Large absorption coefficients come from the band structure of $BaSi_2$, where the localized Ba *d*-like states form flat energy bands in the conduction band.[5–7] Minority-carrier properties, such as a long minority-carrier diffusion length (*ca.*10 μm)[8,9] and a long minority-carrier lifetime (*ca.*10 μs),[10–12] in *a*-axis-oriented undoped n-type $BaSi_2$ epitaxial films spurred interest in this material. One of the striking features of this material is the fact that both large minority-carrier diffusion length and large absorption coefficient are available. This facilitates the collection of photogenerated carriers in $BaSi_2$, and thereby leads to a large photocurrent.

Grain boundaries (GBs) in semiconductor films often deteriorate electrical and optical properties of the films. Therefore, a lot of studies have been conducted on GBs in solar cell materials, such as polycrystalline Si and chalcopyrite semiconductors to improve efficiency.[13–26] One of the powerful tools for studying GBs properties is Kelvin probe force microscopy (KFM) method. Measurements with KFM yield the electrostatic properties of GBs and are used to determine the band diagrams across GBs. KFM revealed that random GBs have negative influences on solar cell performance compared to those with low Σ values in polycrystalline Si,[27,28] and that the electron-hole pairs are well separated at GBs in high-efficiency CIGS solar cells.[29–31] According to our previous work on the potential variations around the GBs using KFM,[32] the potentials were higher at GBs by approximately 30 meV than those in the $BaSi_2$ grain interiors in the undoped n-type $BaSi_2$ films, suppressing the charge carrier recombination at the GBs. This explains the reason why the minority-carrier diffusion length (*ca.*10 μm) is much longer than the average grain size of undoped n-$BaSi_2$ (*ca.*0.2 μm),[8] which is to be an active layer in a $BaSi_2$ pn junction solar cell. Therefore, the potential variations around the GBs are a measure of the minority carrier properties.

A classic solar cell uses a pn junction. Therefore, it is of essential importance to investigate the properties of GBs in impurity-doped n- and p-type semiconductor films.[33,34] Impurity doping of group-III and group-V elements enables us to control the carrier type and conductivity of $BaSi_2$ experimentally.[35–39] Among them, boron (B) and antimony

(Sb) atoms are considered suitable for p- and n-type dopants, respectively, because the carrier concentration can be controlled in a wide range between 10^{17} and $10^{20}\,cm^{-3}$ at room temperature (RT).[35,38]

This article reports on the surface potential variations around the GBs in Sb-doped n-$BaSi_2$ and B-doped p-$BaSi_2$ films, and discusses their dependence on carrier concentrations. We also discussed their densities of states (DOSs) and total energies using first-principles pseudopotential method to clarify the possible insertion sites of impurity atoms, and the reason for the observed n-type conduction in Sb-doped $BaSi_2$ and p-type conduction in B-doped $BaSi_2$. There have been no theoretical reports on what happens when Sb or B atoms are doped into $BaSi_2$. Regarding indium (In) or gallium (Ga) doping into $BaSi_2$, Imai and Watanabe calculated their electronic structures,[40] and found that the In (Ga)-doped $BaSi_2$ was expected to be p-type, and that substitution of Si in the $BaSi_2$ lattice by In (Ga) is more favorable than that of Ba from the energetic point of view.

$BaSi_2$ belongs to the space group of *Pnma*.[41] There are two crystallographically inequivalent sites for Ba ($Ba^{(1)}$ and $Ba^{(2)}$) and three inequivalent sites for Si ($Si^{(3)}$, $Si^{(4)}$, and $Si^{(5)}$) in the unit cell of $BaSi_2$. The unit cell contains eight formula units. Therefore, the stoichiometric description of the unit cell is Ba_8Si_{16}, and the atoms are distributed over $4Ba^{(1)}$, $4Ba^{(2)}$, $4Si^{(3)}$, $4Si^{(4)}$, and $8Si^{(5)}$. Hereafter, we describe the compound, for example, as $Ba_8Sb^{(3)}Si_{15}$, where one of the $Si^{(3)}$ sites of Ba_8Si_{16} is substituted with Sb. The formation energies of the Ba_8Si_{16} substituted with In or Ga were calculated by using the first-principles method.[40] In the case of Ga doping,[40] the formation energies of $Ba_7Ga^{(1)}Si_{16}$ and $Ba_7Ga^{(2)}Si_{16}$ are higher than those of $Ba_8Ga^{(3)}Si_{15}$, $Ba_8Ga^{(4)}Si_{15}$, and $Ba_8Ga^{(5)}Si_{15}$. On the other hand, the energy differences between $Ba_7Ga^{(1)}Si_{16}$ and $Ba_7Ga^{(2)}Si_{16}$ and between $Ba_8Ga^{(3)}Si_{15}$, $Ba_8Ga^{(4)}Si_{15}$, and $Ba_8Ga^{(5)}Si_{15}$ are small. The same was true for In doping.[40] Hence, we chose one $Ba^{(1)}$ site for Ba substitution, and one $Si^{(3)}$ site for Si substitution in this article although there are another Ba site, $Ba^{(2)}$, and the other two Si sites, $Si^{(4)}$ and $Si^{(5)}$, in Ba_8Si_{16}.

II. METHODS

A. Formation of Sb- or B-doped $BaSi_2$ films and characterizations

a-axis-oriented Sb-doped n-type and B-doped p-type $BaSi_2$ epitaxial films were formed on Si(111) by molecular beam epitaxy (MBE). The details of the growth procedure were already reported.[35,38] An ion-pumped MBE system equipped with standard Knudsen cells for Ba, Sb, and B, and an electron-beam evaporation source for Si was used. We adopted the growth condition so that the hole concentration, *p*, in the B-doped $BaSi_2$ becomes much higher than the electron concentration, *n*, in the Sb-doped $BaSi_2$. This is because we plan to use n-$BaSi_2$ as an active layer in a solar cell owing to its long minority-carrier diffusion length,[8,9] and the sharp p^+/n interface due to small diffusion coefficients of B in $BaSi_2$.[42] The value of *n* in the Sb-doped $BaSi_2$ films, samples S1–S3, was controlled by changing the substrate temperature, T_S, as 580, 550, and 520 °C, respectively, while the temperature of Sb crucible, T_{Sb}, was fixed at 250 °C. Undoped n-$BaSi_2$ ($n = 5 \times 10^{15}\,cm^{-3}$) in Ref. 32, was used as sample S0 for comparison. The value of *p* in the B-doped $BaSi_2$ films, samples B1–B3, was controlled by varying the temperature of B crucible, T_B, as 1300, 1400, and 1450 °C, respectively, while T_S was fixed at 650 °C. The sample preparation is summarized in Table I. The carrier concentration was measured at RT by Hall measurement using the van der Pauw method. The crystalline quality of the grown films was characterized by reflection high-energy electron diffraction (RHEED) and x-ray diffraction (XRD) measurements with a Cu Kα source to confirm epitaxial growth of the layers. Surface topographies and potential variations were characterized by Shimazu SPM-9600 atomic force microscopy (AFM) and KFM, respectively. In order to investigate the GBs of $BaSi_2$ and B precipitates, samples for transmission electron microscopy (TEM) observations were prepared by mechanical polishing and ion milling, and their cross sections were observed using TOPCON EM-002B operated at 120 kV.

B. Computational details

We calculated the DOSs and the binding energies of Sb-doped Ba_8Si_{16} and B-doped Ba_8Si_{16} using the VASP code[43] based on the density-functional theory (DFT) with the projector-augmented wave pseudopotential[44] and Perdew-Wang Generalized Gradient Approximations method.[45] The optimized structure of Ba_8Si_{16} is shown in Fig. 1. The total energy minimization was obtained via an optimization of the lattice parameters and a relaxation of the atomic positions in a conjugate gradient routine. The convergence in the total energy was better than 1 meV/atom using the energy cutoff of 600 eV and the $6 \times 8 \times 4$ grid of Monkhorst–Pack points.[46] We also explored the possibility of interstitial compound with $BaSi_2$. There are 16 candidate interstitial sites in the $BaSi_2$ lattice. According to Imai and Watanabe,[47] the most probable insertion sites are the 4*c* sites, where an impurity atom is surrounded by three Si atoms, one of which is at a peak of one Si-tetrahedron and the other two of which are composing an edge of the other Si-tetrahedron. Thus, we chose one of the 4*c* sites, the fractional coordinate of which is (0.5841, 0.25, 0.2251). This compound is described as $Ba_8Si_{16}Sb$. We also calculated the DOSs and the formation energies of aluminum (Al)-doped $BaSi_2$ and In-doped $BaSi_2$

TABLE I. Sample preparation: substrate temperature (T_S), Sb crucible (T_{Sb}) or B crucible temperature (T_B), $BaSi_2$ layer thickness (*t*), and carrier concentration are specified.

Sample	T_S (°C)	T_{Sb} (°C)	T_B (°C)	*t* (nm)	Carrier concentration (cm^{-3})
S0	580	…	…	100	$n = 5 \times 10^{15}$ (undoped)
S1	580	280	…	100	$n = 1.2 \times 10^{17}$
S2	550	280	…	100	$n = 3.2 \times 10^{17}$
S3	520	280	…	200	$n = 1.8 \times 10^{18}$
B1	650	…	1300	100	$p = 2.7 \times 10^{18}$
B2	650	…	1400	100	$p = 4.0 \times 10^{18}$
B3	650	…	1450	100	$p = 2.0 \times 10^{20}$

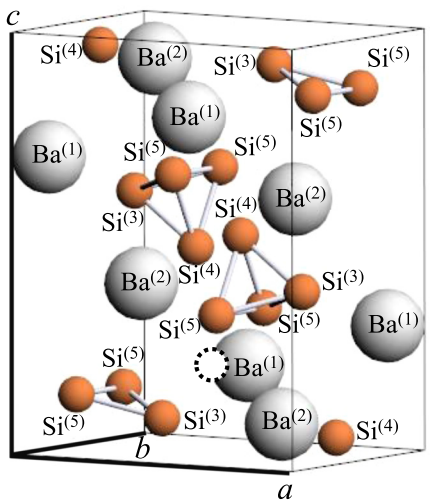

FIG. 1. Optimized structure of Ba_8Si_{16}. An open dotted circle shows the location of an interstitial 4*c* site. The fractional coordinate of the 4*c* site is (0.5841, 0.25, 0.2251).

for comparison. In our framework of first-principles calculations, we cannot take into account thermal effects at the finite temperature to the DFT calculation.

III. RESULTS AND DISCUSSION

A. Calculation results

Table II shows the summary of calculated electronic energies for Ba_8Si_{16} doped with an impurity atom (Sb, B, Al, or In). The binding energy of Ba_8Si_{16} was calculated to be −133.696 eV. The total energy after impurity doping is calculated using the binding energies of the optimized structures as follows. In the case that an Sb atom replaces a Ba atom in the $Ba^{(1)}$ site, the total energy of $Ba_7Sb^{(1)}Si_{16} + Ba$ is given by

$$(-129.389) + (-1.912) = -131.301\,\text{eV}.$$

In another case that an Sb atom replaces a Si atom in the $Si^{(3)}$ site, the total energy of $Ba_8Sb^{(3)}Si_{15} + Si$ is

$$(-132.273) + (-5.417) = -137.690\,\text{eV}.$$

TABLE II. Calculated electronic energies for Sb-doped $BaSi_2$, B-doped $BaSi_2$, Al-doped $BaSi_2$, and In-doped $BaSi_2$.

Compound	Total energy (eV)
$8Ba + 16Si \rightarrow Ba_8Si_{16}$	−133.696
$Ba_8Si_{16} + Sb \rightarrow Ba_7Sb^{(1)}Si_{16} + Ba$	−131.301 (−129.389−1.912)
$Ba_8Si_{16} + Sb \rightarrow Ba_8Sb^{(3)}Si_{15} + Si$	−137.690 (−132.273−5.417)
$Ba_8Si_{16} + Sb \rightarrow Ba_8Si_{16}Sb$	−135.861
$Ba_8Si_{16} + B \rightarrow Ba_7B^{(1)}Si_{16} + Ba$	−132.758 (−130.846−1.912)
$Ba_8Si_{16} + B \rightarrow Ba_8B^{(3)}Si_{15} + Si$	−138.209 (−132.792−5.417)
$Ba_8Si_{16} + B \rightarrow Ba_8Si_{16}B$	−138.999
$Ba_8Si_{16} + Al \rightarrow Ba_7Al^{(1)}Si_{16} + Ba$	−130.609 (−128.697−1.912)
$Ba_8Si_{16} + Al \rightarrow Ba_8Al^{(3)}Si_{15} + Si$	−136.494 (−131.077−5.417)
$Ba_8Si_{16} + Al \rightarrow Ba_8Si_{16}Al$	−135.698
$Ba_8Si_{16} + In \rightarrow Ba_7In^{(1)}Si_{16} + Ba$	−130.420 (−128.508−1.912)
$Ba_8Si_{16} + In \rightarrow Ba_8In^{(3)}Si_{15} + Si$	−135.586 (−130.169−5.417)
$Ba_8Si_{16} + In \rightarrow Ba_8Si_{16}In$	−133.857

In the same way, the total energy of $Ba_8Si_{16}Sb$ is calculated to be −135.861 eV. These results imply that replacement of Si with Sb is most likely to occur in Sb-doped $BaSi_2$ from the energetic point of view. The same assumption can be applied to B-, Al-, or In-doped $BaSi_2$. This result agrees well with Ref. 40. However, in the case of B-doped $BaSi_2$, we note that not only the Si substitution with B but also the interstitial insertion of B into the 4*c* site is energetically favorable. We speculate this difference results from a smaller atomic radius of B than those of Sb, Al, and In.

Figure 2 shows the total DOSs of (a) undoped Ba_8Si_{16}, (b) $Ba_8Sb^{(3)}Si_{15}$, (c) $Ba_8B^{(3)}Si_{15}$, (d) $Ba_8Si_{16}B$, (e) $Ba_8Al^{(3)}Si_{15}$, and (f) $Ba_8In^{(3)}Si_{15}$ near the Fermi level, E_f. The energy zero of the DOS curve is taken at their E_f. As shown in Fig. 2(b), E_f crosses the bottom of the conduction band, E_C, in $Ba_8Sb^{(3)}Si_{15}$, and hence the doped $BaSi_2$ will perform as the n-type. Needless to state, this does not necessarily mean that Sb-doped $BaSi_2$ becomes degenerated. Concentration of the doped element would be much lower in the actual fabrication than that assumed in the present calculations. In contrast, when Si was replaced with B, Al, or In, E_f crosses the top of the valence band, E_V, and the doped $BaSi_2$ will work as the p-type as shown in Figs. 2(c), 2(e), and 2(f), respectively. These results agree well with those experimentally obtained.[35–39] $BaSi_2$ is a Zintl phase compound consisting of an electropositive Ba and an electronegative Si, where the electropositive Ba donates its electrons to

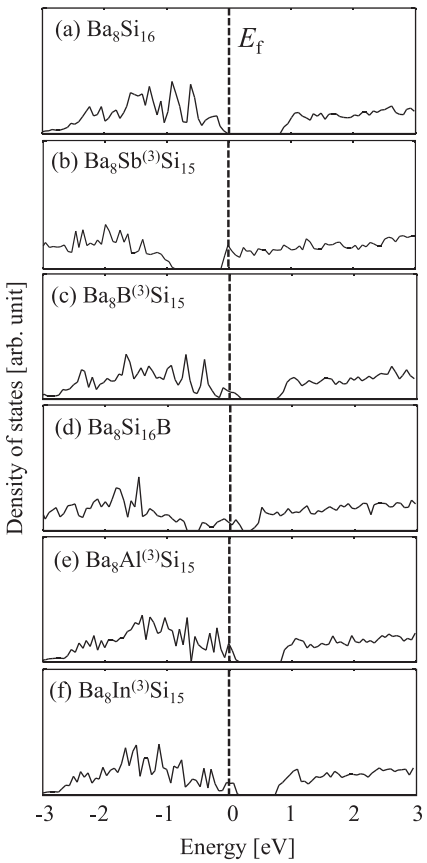

FIG. 2. Total DOSs of (a) undoped Ba_8Si_{16}, (b) $Ba_8Sb^{(3)}Si_{15}$, (c) $Ba_8B^{(3)}Si_{15}$, (d) $Ba_8Si_{16}B$, (e) $Ba_8Al^{(3)}Si_{15}$, and (f) $Ba_8In^{(3)}Si_{15}$ near E_f. The energy zero of the DOS curve is taken at their E_f.

the Si, which uses the electrons in the formation of covalent bonds in Si_4 tetrahedra to satisfy valence.[48] It was confirmed from both theory and experiment that the Si 3*p* state is dominant around E_V in $BaSi_2$.[3,49–51] Thus, replacement of Si with Sb increases valence electron concentration and causes the change of $BaSi_2$ to the n-type, whereas replacement of Si with B, Al, or In decreases it, and forms the p-type. However, localized states appear in the band gap of $Ba_8Si_{16}B$ as shown in Fig. 2(d). Thus, it is difficult to clarify the conductivity type of this compound.

B. GBs in Sb-doped n-$BaSi_2$

We observed streaky RHEED patterns, and *a*-axis-oriented diffraction peaks in the θ-2θ XRD patterns for all the samples. These results show that *a*-axis oriented $BaSi_2$ films doped with Sb and those with B atoms were formed on Si(111). As summarized in Table I, we fabricated Sb-doped n-$BaSi_2$ films with n ranging from $n = 1.2 \times 10^{17}$ to $n = 1.8 \times 10^{18}\,cm^{-3}$ and B-doped $BaSi_2$ films with p ranging from $p = 2.7 \times 10^{18}\,cm^{-3}$ to $p = 2.2 \times 10^{20}\,cm^{-3}$. The carrier concentrations increased significantly in the impurity doped-$BaSi_2$ compared with undoped one, sample S0.

Figures 3(a)(a′)–3(d)(d′) show the AFM topographic and KFM potential images, measured for samples S0–S3, respectively, with their cross sectional profiles along white broken lines in the same areas. The positions of GBs are indicated by colored lines in the cross sectional profiles. We see that the potentials at the GBs are higher than those of grain interiors for sample S0 in Figs. 3(a) and 3(a′). This means that the GBs are positively charged. This result shows that band bending occurs downwards at GBs as shown in Fig. 4(a′). This tendency was also observed in other Sb-doped n-$BaSi_2$ films, samples S1 and S2 in Figs. 4(b′) and 4(c′), except sample S3. The downward band bending in n-type $BaSi_2$ is beneficial for the suppression of recombination of minority carriers (holes). These holes experience a repelling force near the GBs. In contrast, the potentials are smaller at the GBs than those of the grain interiors in sample S3, meaning that the GBs are negatively charged.

Next, we evaluated the potential barrier height, ΔE_{GB}, at GBs by

$$\Delta E_{GB} = -q(V_{GB} - V_{G,ave}), \tag{1}$$

where V_{GB} and $V_{GB,ave}$ are the potential at GBs and the average potential in the inner parts of two adjoining grains, respectively. The symbol q denotes the elementary charge. The same procedure was repeated for approximately 30 GBs in each sample. The histograms of barrier height are shown in Figs. 4(a)–4(d). The barrier height for holes (minority-carriers) was positive for samples S0–S2 in Figs. 4(a′)–4(c′), and negative for sample S3 in Fig. 4(d′). The average barrier height for holes was approximately 30 meV for sample S0, and 10 meV or smaller for samples S1 and S2. On the other hand, the average barrier height for electrons was approximately 15 meV for sample S3. Minority-carriers (holes) are attracted by the electric fields towards the GBs and thereby may recombine at the GBs in this case. However, these barrier heights are almost the same as the thermal energy of 26 meV

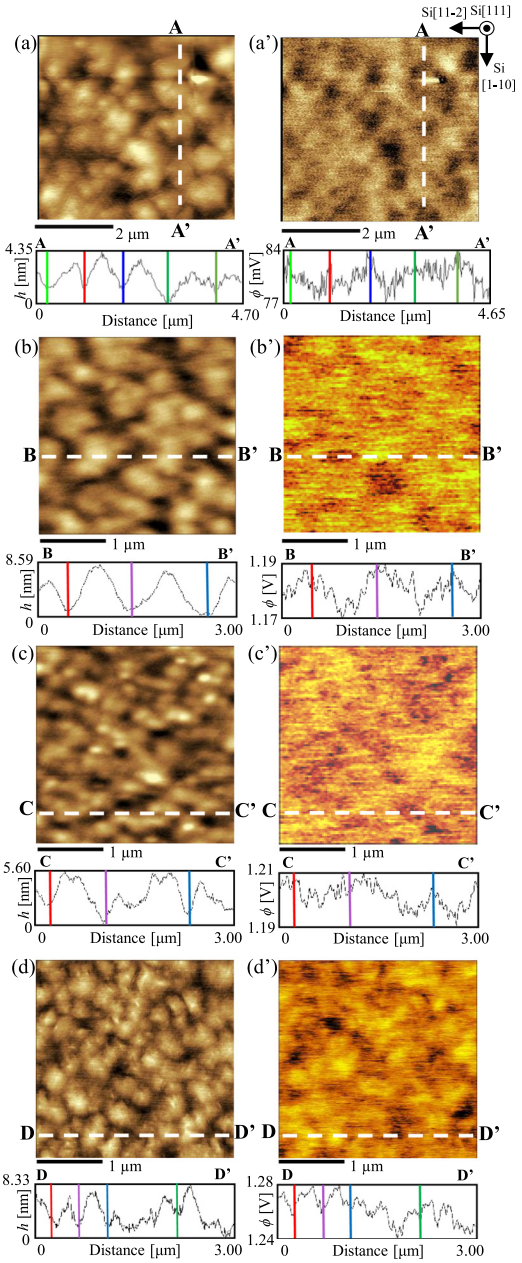

FIG. 3. (a)–(d) AFM topographic and (a′)–(d′) KFM potential images with their cross sections along white broken lines for samples S0–S3, respectively. (a) and (a′) show the results obtained for undoped $BaSi_2$. Reprinted with permission from M. Baba *et al.*, Appl. Phys. Lett. **103**, 142113 (2013). Copyright 2013 AIP Publishing LLC.

at RT (25 °C). Thus, we may expect that such small barrier heights observed in samples S0–S3 do not deteriorate carrier transport properties. Note that more heavily doping of Sb may increase attractive electric fields for holes towards the GBs, leading to recombination. Therefore, n should be designed as small as possible for use as an active layer.

The band diagram across the GBs facilitates an estimate of the area density of charges at GBs, σ_{GB}. We take here sample S0, for example, and derive σ_{GB} in one dimensional approximation. The positive charge σ_{GB} at the GBs is shielded by the negative charge consisting of majority carriers (electrons) in the band bending region with a width $2W$. The electron concentration $n(x)$ at a position x $(0 \le x \le W)$ from the GB is given by the following Poisson's equation:

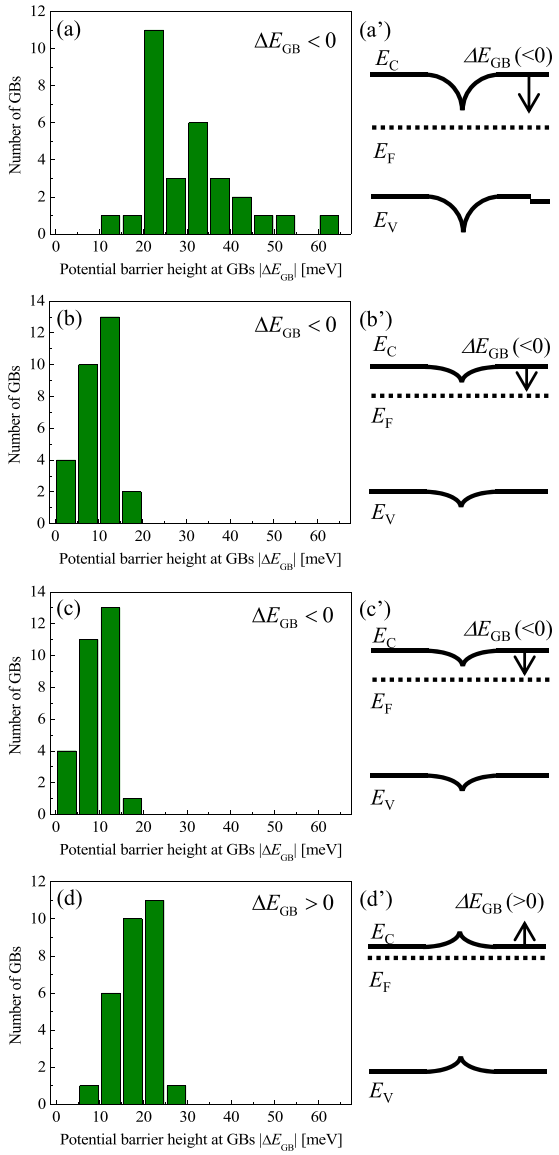

FIG. 4. Histograms of barrier height at GBs for samples (a) S0, (b) S1, (c) S2, and (d) S3. Schematic band diagrams across the GB are also shown in (a′)–(d′).

$$\frac{d^2}{dx^2}\phi(x) = \frac{qn(x)}{\varepsilon_0 \varepsilon_r}, \tag{2}$$

$$n(x) = n \exp\left[\frac{q\phi(x)}{k_B T}\right]. \tag{3}$$

Here, $\phi(x)$ is the potential with respect to the grain interior, where there is no band bending, ε_0 the dielectric constant of vacuum, $\varepsilon_r = 16$ the dielectric permeability of $BaSi_2$,[52] k_B the Boltzmann constant, $n = 5 \times 10^{15}\,\mathrm{cm}^{-3}$, and T the absolute temperature. Equation (2) can be solved numerically using two boundary conditions, that is, $\phi(0) = 30\,\mathrm{mV}$ and $\phi(W) = 0\,\mathrm{mV}$. Numerical simulations show that the barrier height at $x = 0$ reaches 30 meV when W is 120 nm. The value $W \approx 100\,\mathrm{nm}$ matches well to the cross section in Fig. 3(a′). The area density of charges σ_{GB} present at the GBs is thus obtained by using charge neutrality[20]

$$\sigma_{GB} = 2\int_0^W n(x)dx \approx 2 \times 10^{11}\,\mathrm{cm}^{-2}. \tag{4}$$

σ_{GB} was also calculated to be of the order of $10^{11}\,\mathrm{cm}^{-2}$ in samples S1 and S2. In the case of sample S3, the negative sheet charge at the GBs is compensated by the positively charged space-charge region with a width $2W$. Assuming complete ionization of Sb atoms and their uniform distribution in the grain interiors, σ_{GB} is given by[20]

$$\sigma_{GB} = 2WN_D^+ = 2Wn \approx 10^{13}\,\mathrm{cm}^{-2} \tag{5}$$

for $W \approx 100\,\mathrm{nm}$. Here, N_D^+ is the ionized Sb concentration. One explanation for the negative charge at the GBs is that the electrons supplied from the heavily Sb-doped n-$BaSi_2$ grain interiors to the GBs outnumbered the positive charges in samples S0–S2, giving rise to the band diagram as shown in Fig. 4(d′).

The change of barrier height is explained at least qualitatively, assuming that E_f is pinned at GBs, whereas E_f approaches the bottom of the conduction band, E_C, in the $BaSi_2$ grain interiors with increasing n. The cause for the downward band bending in the undoped n-$BaSi_2$, sample S0, is explained as follows. The GBs in the *a*-axis-oriented $BaSi_2$ films are mostly composed of $BaSi_2$(011)/(0–11) planes, and on these planes Ba atoms are dominant. Detailed discussions were given in Ref. 8. In the *a*-axis-oriented $BaSi_2$ films on Si(111), there are three epitaxial variants rotating by 120° with each other around the surface normal. In the course of the epitaxial growth of *a*-axis-oriented $BaSi_2$, the (011) plane of one $BaSi_2$ grain coalesces with the (0–11) plane of another $BaSi_2$ grain by lateral growth, forming the GBs. Thus, it is reasonable to think that the GBs are in excess of Ba atoms compared with the $BaSi_2$ grain interiors. Due to the difference in electronegativity between Ba and Si, the Ba atoms are positively charged, and the Si_4 tetrahedra are negatively charged in $BaSi_2$. We speculate that is why the potentials are higher at the GBs than those in the grain interiors of the undoped $BaSi_2$. Regarding Sb-doped n-$BaSi_2$, Si atoms are favorably replaced with Sb atoms as discussed in Table I, and thus E_f approaches E_C with increasing n. However, this is not likely to occur at the GBs because Ba atoms are dominant. This might be the cause of the observed change in barrier height.

We next discuss the barrier height at GBs. The effective density of states in the conduction band, N_C, is approximately $2.6 \times 10^{19}\,\mathrm{cm}^{-3}$ from the principle-axis components of the effective mass tensor for electrons and four equivalent valleys at E_C.[3] The E_C–E_f are calculated to be approximately 0.22, 0.14, 0.11, and 0.07 eV for samples S0–S3, respectively, from the equation

$$E_C - E_f = k_B T \ln\left(\frac{N_C}{n}\right) \tag{6}$$

using their n values. Considering that the average barrier height for holes is approximately 30, 10, and 10 meV in samples S0–S2, and that for electrons is approximately 15 meV in sample S3, the values of E_C–E_f are estimated to be approximately 0.19, 0.13, 0.1, and 0.09 eV, respectively, at the GBs. This discussion clearly shows that the slight change of E_f is necessary to occur at the GBs to account for the observed change in barrier height. We think that defect states

exist at GBs, and the position of E_f at the GBs is changed according to the degree of occupancy of those states by electrons.[53]

C. GBs in B-doped p-$BaSi_2$

Next, we discuss B-doped p-$BaSi_2$. Figures 5(a)(a′)–5(c)(c′) show the AFM topographic and KFM potential images, measured for samples B1–B3, respectively. Their cross sectional profiles along white broken lines in the same areas are also shown. The positions of colored lines correspond to those of GBs. We see that the potentials at the GBs are smaller than those in the $BaSi_2$ grains, indicating that the GBs are negatively charged compared with the grain interiors, and thereby band bending occurs upwards at the GBs as shown in Figs. 6(a) and 6(b). The upward band bending in p-type $BaSi_2$ is favorable for the suppression of recombination of minority carriers (electrons). These electrons are not attracted towards the GBs in samples B1 and B2. Regarding sample B3, it was difficult to distinguish the position of GBs from AFM. However, it is safe to state at least that the potential variations became smaller with increasing p as shown in Figs. 5(a′)–5(c′). The negative charge at the GBs is shielded by the majority carriers (holes) in the band bending region with a width $2W$. Using similar equations like Eqs. (2)–(4), σ_{GB} was calculated to be of the order of $10^{15}\,cm^{-2}$ for samples B1 and B2.

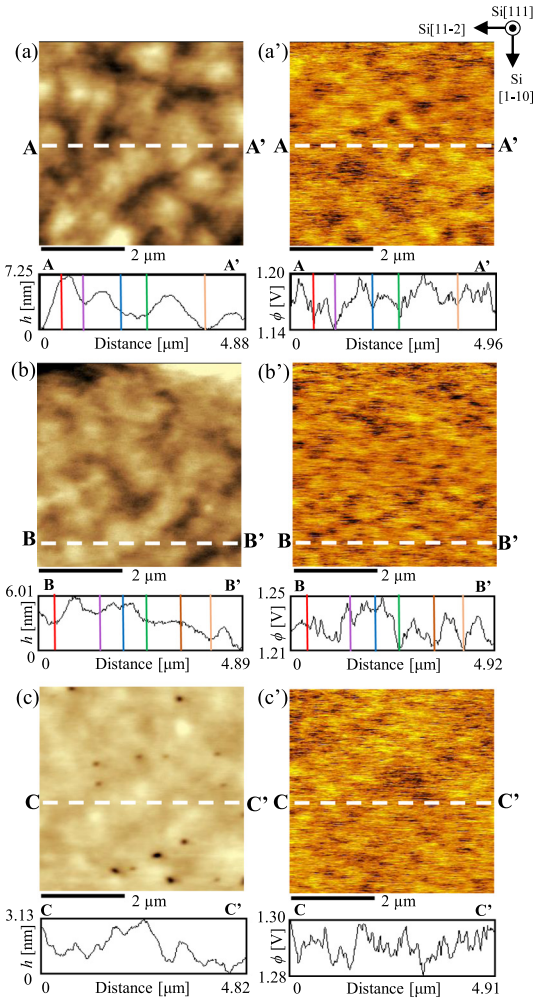

FIG. 5. (a)–(c) AFM topographic and (a′)–(c′) KFM potential images with their cross sections along white broken lines for samples B1–B3, respectively.

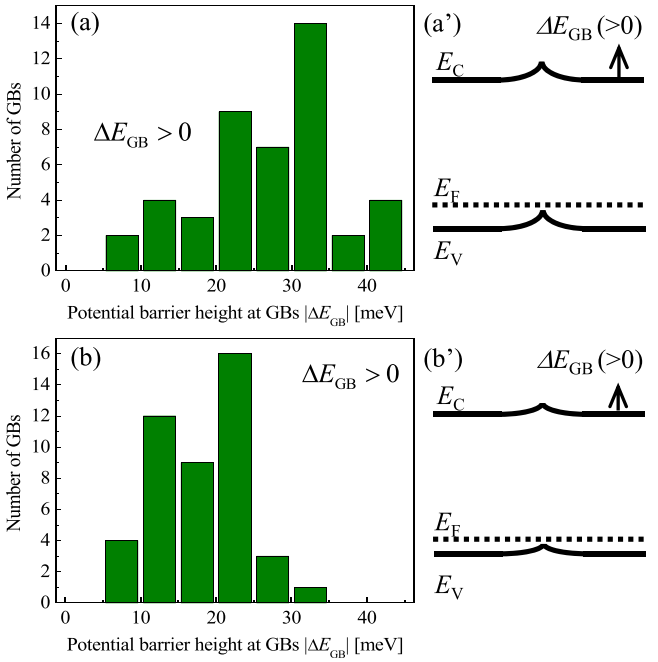

FIG. 6. Histograms of barrier height at GBs for samples (a) B1 and (b) B2. Schematic band diagrams across the GB are also shown in (a′) and (b′).

Next, we evaluated the potential barrier height ΔE_{GB} for electrons at GBs using Eq. (1) for samples B1 and B2. The histograms of barrier height at GBs are shown in Fig. 6. The average barrier height was decreased from approximately 25 meV in sample B1 to 15 meV in sample B2. Such small barrier heights also may not disturb the carrier transport properties across the GBs in B-doped $BaSi_2$. The change of barrier height is explained qualitatively under the assumption that E_f is pinned at the GBs while E_f in the grain interiors approached E_V with increasing p by replacement of Si atoms in the $BaSi_2$ with B atoms. The effective density of states in the valence band, N_V, is approximately $2.0 \times 10^{19}\,cm^{-3}$ from the principal-axis components of the effective mass tensor for holes and two equivalent valleys at E_V.[3] The E_f–E_V are calculated to be approximately 0.05 and 0.04 eV for samples B1 and B2, respectively, from

$$E_f - E_V = k_B T \ln\left(\frac{N_V}{p}\right). \tag{7}$$

Considering that the upward band bending occurs even for sample B2 ($p = 4.0 \times 10^{18}\,cm^{-3}$), E_F seems to be located very close to E_V at the GBs as shown in Figs. 6(a′) and 6(b′). Regarding the different positions of E_f in p-$BaSi_2$ from that in n-$BaSi_2$, we interpret that this result comes from emptying the defect states at the GBs by heavily B doping. Figure 7 shows the bright-field TEM cross section of a 0.53-μm-thick B-doped p-$BaSi_2$ layer on undoped $BaSi_2$/Si(111) grown by MBE using the same growth condition as sample B3. We see lots of B precipitates gathering along the GBs indicated by white arrows. This result suggests that $BaSi_2$ around the GBs

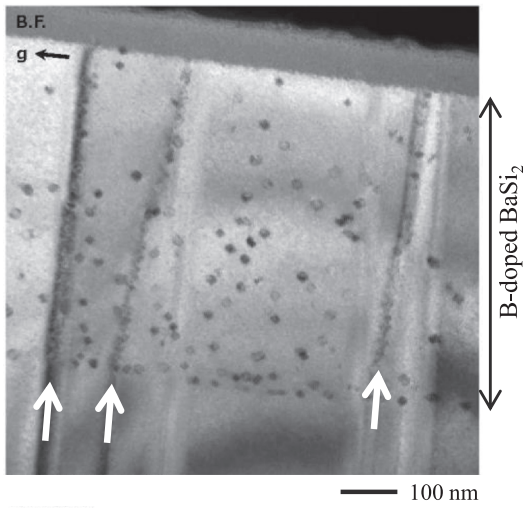

FIG. 7. Bright-field TEM cross sectional image of a 0.53-μm-thick B-doped $BaSi_2$ layer grown by MBE using the same growth condition as sample B3. The layer was formed on undoped $BaSi_2$/Si(111). White arrows show the positions of GBs.

is supposed to be more heavily doped with B atoms than in the grain interiors, forming p^+-$BaSi_2$, and thereby resulting in E_f being close to E_V at the GBs. In other words, the defect states are almost emptied. Another possibility is that such heavily B doping may increase B atoms located at the interstitial sites as discussed in Table II, leading to the formation of localized states within the band gap of $BaSi_2$ as shown in Fig. 2(d), where E_f is almost pinned.

IV. CONCLUSION

We have evaluated the potential variations at the GBs in *a*-axis-oriented Sb-doped n-$BaSi_2$ and B-doped p-$BaSi_2$ epitaxial films by KFM, and compared them with those in undoped n-$BaSi_2$. In the Sb-doped n-$BaSi_2$ films, the band bending occurred downwards at the GBs and the average barrier height for holes was approximately 10 meV when n was 1.2×10^{17} and 3.2×10^{17} cm^{-3}. This downward band bending changed to the upward band bending with a barrier height of approximately 15 meV when n was increased to 1.8×10^{18} cm^{-3}. Much higher Sb doping may induce stronger attractive electric fields for holes (minority carriers) towards the GBs. Thus, n-type doping should be designed as small as possible for use as an active layer. In the B-doped p-$BaSi_2$ films, the potential variations became smaller with increasing p. Upward band bending was observed when p was of the order of 10^{18} cm^{-3}. The average barrier height for electrons decreased from approximately 25 to 15 meV when p was increased from 2.7×10^{18} to 4.0×10^{18} cm^{-3}. In both Sb-doped n-$BaSi_2$ and B-doped p-$BaSi_2$ films, the change of barrier height was explained under the assumption that E_f was varied depending on the degree of occupancy of the defect states at the GBs, while E_f approached E_C or E_V in the $BaSi_2$ grain interiors with increasing carrier concentrations. First-principles calculations revealed that Si substitution with Sb is energetically favorable and forms n-type $BaSi_2$. In the case of B-doped $BaSi_2$, Si substitution with B forms p-type $BaSi_2$; however, the interstitial insertion of B atoms at the 4*c* site is also energetically favorable. The interstitial insertion induces localized states in the band gap.

ACKNOWLEDGMENTS

The authors thank Dr. N. Yoshizawa and Mr. N. Saito of the National Institute of Advanced Industrial Science and Technology for their TEM observations. This work was financially supported in part by Core Research for Evolutionary Science and Technology (CREST) of the Japan Science and Technology Agency.

[1]K. Morita, Y. Inomata, and T. Suemasu, Thin Solid Films **508**, 363 (2006).
[2]K. Toh, T. Saito, and T. Suemasu, Jpn. J. Appl. Phys. Part 1 **50**, 068001 (2011).
[3]D. B. Migas, V. L. Shaposhnikov, and V. E. Borisenko, Phys. Status Solidi B **244**, 2611 (2007).
[4]M. Kumar, N. Umezawa, and M. Imai, J. Appl. Phys. **115**, 203718 (2014).
[5]Y. Imai, A. Watanabe, and M. Mukaida, J. Alloys Compd. **358**, 257 (2003).
[6]Y. Imai and A. Watanabe, Thin Solid Films **515**, 8219 (2007).
[7]M. Kumar, N. Umezawa, and M. Imai, Appl. Phys. Express **7**, 071203 (2014).
[8]M. Baba, K. Toh, K. Toko, N. Saito, N. Yoshizawa, K. Jiptner, T. Sakiguchi, K. O. Hara, N. Usami, and T. Suemasu, J. Cryst. Growth **348**, 75 (2012).
[9]M. Baba, K. Watanabe, K. O. Hara, K. Toko, T. Sekiguchi, N. Usami, and T. Suemasu, Jpn. J. Appl. Phys. Part 1 **53**, 078004 (2014).
[10]K. O. Hara, N. Usami, K. Toh, M. Baba, T. Toko, and T. Suemasu, J. Appl. Phys. **112**, 083108 (2012).
[11]K. O. Hara, N. Usami, K. Nakamura, R. Takabe, M. Baba, K. Toko, and T. Suemasu, Appl. Phys. Express **6**, 112302 (2013).
[12]R. Takabe, K. O. Hara, M. Baba, W. Du, N. Shimada, K. Toko, N. Usami, and T. Suemasu, J. Appl. Phys. **115**, 193510 (2014).
[13]C. H. Seager and G. E. Pike, Appl. Phys. Lett. **35**, 709 (1979).
[14]J. J. J. Yang, P. D. Dapkus, R. D. Dupuis, and R. D. Yingling, J. Appl. Phys. **51**, 3794 (1980).
[15]M. Spencer, R. Stall, L. F. Eastman, and C. E. C. Wood, J. Appl. Phys. **50**, 8006 (1979).
[16]J. Werner, W. Jantsch, and H. J. Queisser, Sol. State Commun. **42**, 415 (1982).
[17]D. P. Joshi and D. P. Bhatt, Sol. Energy Mater. Sol. Cells **22**, 137 (1991).
[18]R. Rizk and G. Nouet, Interface Sci. **4**, 303 (1997).
[19]J. Chen, T. Sekiguchi, D. Yang, F. Yin, K. Kido, and S. Tsurekawa, J. Appl. Phys. **96**, 5490 (2004).
[20]G. Hanna, T. Glatzel, S. Sadewasser, N. Ott, H. P. Strunk, U. Rau, and J. H. Werner, Appl. Phys. A **82**, 1 (2006).
[21]D. R. Kim, C. H. Lee, J. M. Weisse, I. S. Cho, and X. Zheng, Nano Lett. **12**, 6485 (2012).
[22]M. J. Hetzer, Y. M. Strzhemechny, M. Gao, M. A. Contreras, A. Zunger, and L. J. Brillson, Appl. Phys. Lett. **86**, 162105 (2005).
[23]M. Gloeckler, J. R. Sites, and W. K. Metzger, J. Appl. Phys. **98**, 113704 (2005).
[24]M. Kawamura, T. Yamada, N. Suyama, A. Yamada, and M. Konagai, Jpn. J. Appl. Phys. Part 1 **49**, 062301 (2010).
[25]S. Oonishi, M. Kawamura, N. Takano, D. Hashimoto, A. Yamada, and M. Konagai, Thin Solid Films **519**, 7347 (2011).
[26]T. Minemoto, Y. Wakisaka, and H. Takakura, Jpn. J. Appl. Phys. Part 1 **50**, 031203 (2011).
[27]S. Tsurekawa, K. Kido, and T. Watanabe, Philos. Mag. Lett. **85**, 41 (2005).
[28]S. Tsurekawa, K. Kido, and T. Watanabe, Mater. Sci. Eng., A **462**, 61 (2007).
[29]C.-S. Jiang, R. Noufi, J. A. AbuShama, K. Ramanathan, H. R. Moutinho, J. Pankow, and M. M. Al-Jassim, Appl. Phys. Lett. **84**, 3477 (2004).
[30]D. F. Marrón, S. Sadewasser, A. Meeder, Th. Glatzel, and M. Ch. Lux-Steiner, Phys. Rev. B **71**, 033306 (2005).
[31]M. Takihara, T. Minemoto, Y. Wakisaka, and T. Takahashi, Prog. Photovoltaics **21**, 595 (2013).

[32]M. Baba, S. Tsurekawa, K. Watanabe, W. Du, K. Toko, K. O. Hara, N. Usami, T. Sekiguchi, and T. Suemasu, Appl. Phys. Lett. **103**, 142113 (2013).
[33]D. A. Bonnell, B. Huey, and D. Carroll, Solid State Ionics **75**, 35 (1995).
[34]S. Sabuktagin, M. A. Reshchikov, D. K. Johnstone, and H. Morkoç, Mater. Res. Soc. Symp. Proc. **798**, Y5.39 (2003).
[35]M. Kobayashi, Y. Matsumoto, Y. Ichikawa, D. Tsukada, and T. Suemasu, Appl. Phys. Express **1**, 051403 (2008).
[36]M. Takeishi, Y. Matsumoto, R. Sasaki, T. Saito, and T. Suemasu, Phys. Proc. **11**, 27 (2011).
[37]M. Ajmal Khan, T. Saito, K. Nakamura, M. Baba, W. Du, K. Toko, and T. Suemasu, Thin Solid Films **522**, 95 (2012).
[38]M. Ajmal Khan, K. O. Hara, W. Du, M. Baba, K. Nakamura, M. Suzuno, K. Toko, N. Usami, and T. Suemasu, Appl. Phys. Lett. **102**, 112107 (2013).
[39]M. Ajmal Khan, K. Nakamura, W. Du, K. Toko, N. Usami, and T. Suemasu, Appl. Phys. Lett. **104**, 252104 (2014).
[40]Y. Imai and A. Watanabe, Intermetallics **15**, 1291 (2007).
[41]J. Evers, J. Solid State Chem. **32**, 77 (1980).
[42]K. Nakamura, M. Baba, M. Ajmal Khan, W. Du, M. Sasase, K. O. Hara, N. Usami, K. Toko, and T. Sueamsu, J. Appl. Phys. **113**, 053511 (2013).
[43]G. Kresse and D. Joubert, Phys. Rev. B **59**, 1758 (1999).
[44]P. E. Blöchl, Phys. Rev. B **50**, 17953 (1994).
[45]J. Perdew and Y. Wang, Phys. Rev. B **45**, 13244 (1992).
[46]H. J. Monkhorst and J. D. Pack, Phys. Rev. B **13**, 5188 (1976).
[47]Y. Imai and A. Watanabe, Intermetallics **19**, 1102 (2011).
[48]S. M. Kauzlarich, *Chemistry, Structure, and Bonding of Zintl Phases and Ions*, 1st ed. (Wiley-VCH, 1996).
[49]Y. Imai and A. Watanabe, Intermetallics **10**, 333 (2002).
[50]S. Kishino, T. Imai, T. Iida, Y. Nakanishi, M. Shinada, Y. Takanashi, and N. Hamada, J. Alloys Compd. **428**, 22 (2007).
[51]M. Baba, K. Ito, W. Du, T. Sanai, K. Okamoto, K. Toko, S. Ueda, Y. Imai, A. Kimura, and T. Suemasu, J. Appl. Phys. **114**, 123702 (2013).
[52]N. A. A. Latiff, T. Yoneyama, T. Shibutami, K. Matsumaru, K. Toko, and T. Suemasu, Phys. Status Solidi C **10**, 1759 (2013).
[53]A. Many, Y. Goldstein, and N. B. Grover, *Semiconductor Surfaces*, 1st ed. (North-Holland, Amsterdam, 1965).